Multifunctional Sensor Based on Translational-Rotary Triboelectric Nanogenerator

Zhiyi Wu, Binbin Zhang, Haiyang Zou, Zhiming Lin, Guanlin Liu, and Zhong Lin Wang*

Triboelectric nanogenerators with a large number of desirable advantages, such as flexibility, light weight, and easy integration, are unique for sensor design. In this paper, based on the triboelectric nanogenerator (TENG), a cylindrical self-powered multifunctional sensor (MS) with a translational-rotary magnetic mechanism is proposed, which has the capacity to detect acceleration, force, and rotational parameters. The MS can transform a translational motion into a swing motion or a multicircle rotational motion of a low damping magnetic cylinder around a friction layer and hence drives the TENG to generate voltages output. For enhancing the output performance of the TENG, an electrode material with small work function, low resistance, and suitable surface topography is the best choice. According to the structure characteristic of the translational-rotary magnetic mechanism, the MS can easily respond to a weak striking and can be used to measure the rotational parameters without the need of coaxial installation. Based on the MS, some applications are established, for example measuring the punch acceleration of a boxer, the hitting force and swing angle of golf club, which demonstrate the feasibility and efficiency of the MS and exhibit that the MS could find applications in sports.

Nowadays, the concepts of smart city, smart transportation, smart home, etc. are emerging lifestyle, which shows that the Internet of Things (IoTs) technology is becoming more and more mature. With a rapid development of IoTs, the demands of system integration, intelligent, and miniaturization have expedited research on multifunctional sensors.[1–5] Due to the MEMS technology, the existing commercial sensors include accelerometers,[6,7] gyroscopes,[8] and compasses[9] gain enormous success. Despite the superior performance and the small size, the commercial ones are usually of single function. However, the union of some unitary functional sensors that virtually run independently is the most common technical approach

Prof. Z. Y. Wu, Prof. Z. L. Wang
Beijing Institute of Nanoenergy and Nanosystems
Chinese Academy of Sciences
Beijing 100085, China
E-mail: zlwang@binn.cas.cn
Prof. Z. Y. Wu, Dr. B. B. Zhang, Dr. H. Y. Zou, Dr. Z. M. Lin, Dr. G. L. Liu, Prof. Z. L. Wang
School of Materials Science and Engineering
Georgia Institute of Technology
Atlanta, GA 30332-0245, USA

to the current multifunctional sensors. On the other hand, IoTs also expects the sensors can continuously work for long hours without maintenance.[10] The energy harvesting technologies that can provide continuous power supply[11–16] and self-powered sensors that can directly transfer the detect information into electrical signals even without power[7,17,18] are the idea approaches to meet the requirements.

Based on the triboelectric effect and the electrostatic induction, triboelectric nanogenerators (TENGs) invented by Wang and co-workers[19] have a few remarkable advantages, such as flexibility, light weight, easy integration. They have demonstrated to be an applicable solution for both self-powered sensing and energy harvesting.[20–23] Specifically, the force,[24] speed,[25,26] acceleration,[27,28] direction,[29] and angle[30] all can be measured by the TENG. And the TENG also has been successfully used to build multifunctional sensors.[31–33] Based on the TENG, a real multifunctional sensor enabled by magnetically regulated TENG has the capacity to measure motion parameters, including acceleration, speed, and direction of rotary and linear motions.[33] Unfortuately, six output channels increace the complexity of the sensor and the surface contact friction limits its sensitivity. Moreover, for enhancing the output performance of the TENG, many works are focused on the selection and the surface nanocrystallization of friction materials, which both are relatead to the triboelectric effect.[34–36] However, about the electrostatic induction, there also need some theoretical guidances of the electrode materials selection.

In this paper, inspired by the movement statement of a magnetic cylinder placed beside a fixed magnetic cylinder, a cylindrical self-powered multifunctional sensor (MS) with a translational-rotary magnetic mechanism is presented, which is capable of detecting acceleration, force, and rotational parameters. The MS is composed of a translational-rotary magnetic mechanism, a TENG module, and an acrylic shell. The translational-rotary magnetic mechanism is a low damping magnetic cylinder (MC) rotating around a fixed circular tube, which is embedded by a magnetic disk (MD). The sensitivity of the MS can be adjusted by changing the distance between two magnets. The TENG module consists of the MC and a friction layer that is a polytetrafluoroethylene (PTFE) film with two interdigitated electrodes (IEs) bonded on the surface of the tube. The MS can transform a translational motion into a swing motion or a
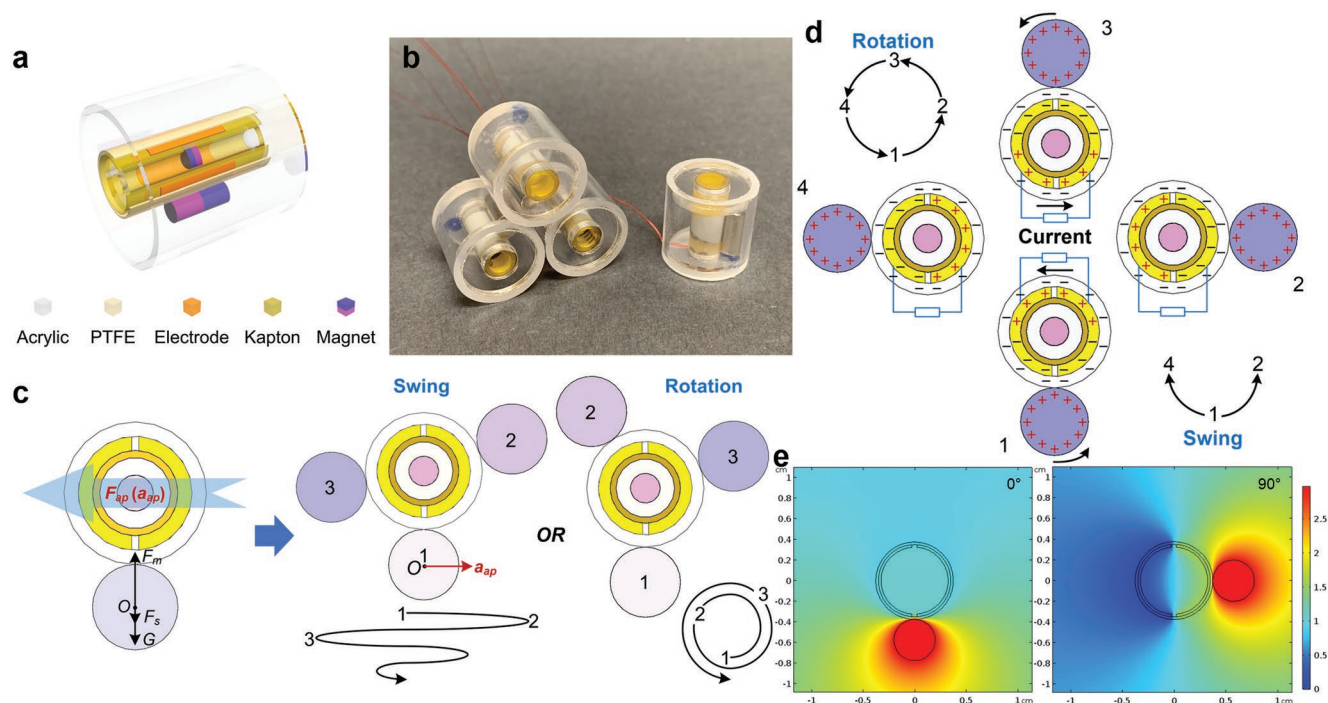
ADVANCED
SCIENCE NEWS
www.advancedsciencenews.com

ADVANCED
ENERGY
MATERIALS
www.advenergymat.de

Figure 1. Structural design and working principle of the MS. a) Schematic illustration of the MS. b) Entities of the MS. c) Mechanical analysis. d) Schematic of charge distribution. e) Electrostatic potential distributions at two typical positions.

multicircle rotational motion of the MC around the PTFE film and hence drives the electrodes to generate voltages output. So, from the electrodes' output waveforms, amplitude, frequency, and some time features can be extracted to determine the excitation parameters. For providing a theoretical guidance of the electrode material selection, the output performances with the electrode material of different work function, resistance, and surface topography are tested. The influence of the pairs of IEs on the output performace is studied. Based on the MS, some boxing, golf, and vehicle safety applications are explored to prove the effectiveness and feasibility of the MS.

The structure diagram of the translational-rotary triboelectric nanogenerator-based multifunctional sensor are shown in **Figure 1**a and Figure S1 (Supporting Information). Figure 1b is a photograph of the MS, the height and diameter of which are both 19 mm. Its volume is about 5.38 cm³. The skeletons of the MS are formed by two tubes and two covers, all of which are central symmetry and made of acrylic. It provides a ring cavity to place the low damping magnetic cylinder, which is attracted by the magnetic disk embedded in the small tube. The height, inner, and outer diameters of the cavity are 13 mm, 6.65 mm, and 15.9 mm, respectively. The dimensions of two magnets (Ni plating, NdFeB, N38) are 10 mm × 4 mm and 1 mm × 2.54 mm. The TENG module consists of the MC and a friction layer that is a PTFE film with two IEs bonded on the surface of the small tube. The width of the gaps between the electrodes is 0.5 mm. Under the role of the magnetic attractive force between two magnets, the MC is bound around the friction layer. The mechanical analysis illustration of the MS is described in Figure 1c. Without excitations, the MC will be always under the MD due to the gravity (G). To make sure the MS has a good sensitivity, the magnetic force between the two

magnets (F_m) should be a little larger than G. Then, the friction layer applies a supporting force (F_s) to the MC ($G + F_s = F_m$). F_m can be adjusted by changing the space between two magnets (d_m). Owing to the limitation of prepared acrylic tubes (Figure 1b), d_m is assigned as 5.33 mm. When the MS is suffered by an excitation (F_{ap} (a_{ap})), under the combined action of inertia and F_m and choosing the friction layer as the reference frame, the MC will be applied an acceleration along the opposite direction to swing around the friction layer. When F_{ap} (a_{ap}) is larger enough, the MC can rotate around the friction layer for many circles and then into the swing stage. In these processes, based on the triboelectric effect, a short-circuit current (I_{sc}) can be perceived on the electrodes, as shown in Figure 1d that illustrates the charge distributions of the MS. With the MC swings around the friction layer, due to the triboelectric polarity difference between PTFE and Ni, electrons will transfer from Ni to PTFE. Then, it causes the PTFE and Ni with negative and positive charges in the saturated state, respectively. On their surfaces, the charges cannot be neutralized or conducted away in the testing process. Thus, the Ni covering the MC can be considered as an equipotential surface. Then, according to the electrostatic induction, the I_{sc} will be changed with the locomotion of the MC. Figure 1e describes the simulation results using the COMSOL Multiphysics 5.3 of two typical electrostatic voltage distributions with the MC on the 0° and 90° positions. When the MC is on the 0° position, two electrodes have the same electrostatic voltage distributions. When the MC is on the 90° position, the right and the left electrodes reach the maximum and minimum values, respectively. The simulation results of the MC rotating around the friction layer are recorded in Video S1 (Supporting Information). These show the electrostatic potential distribution difference between the two electrodes.
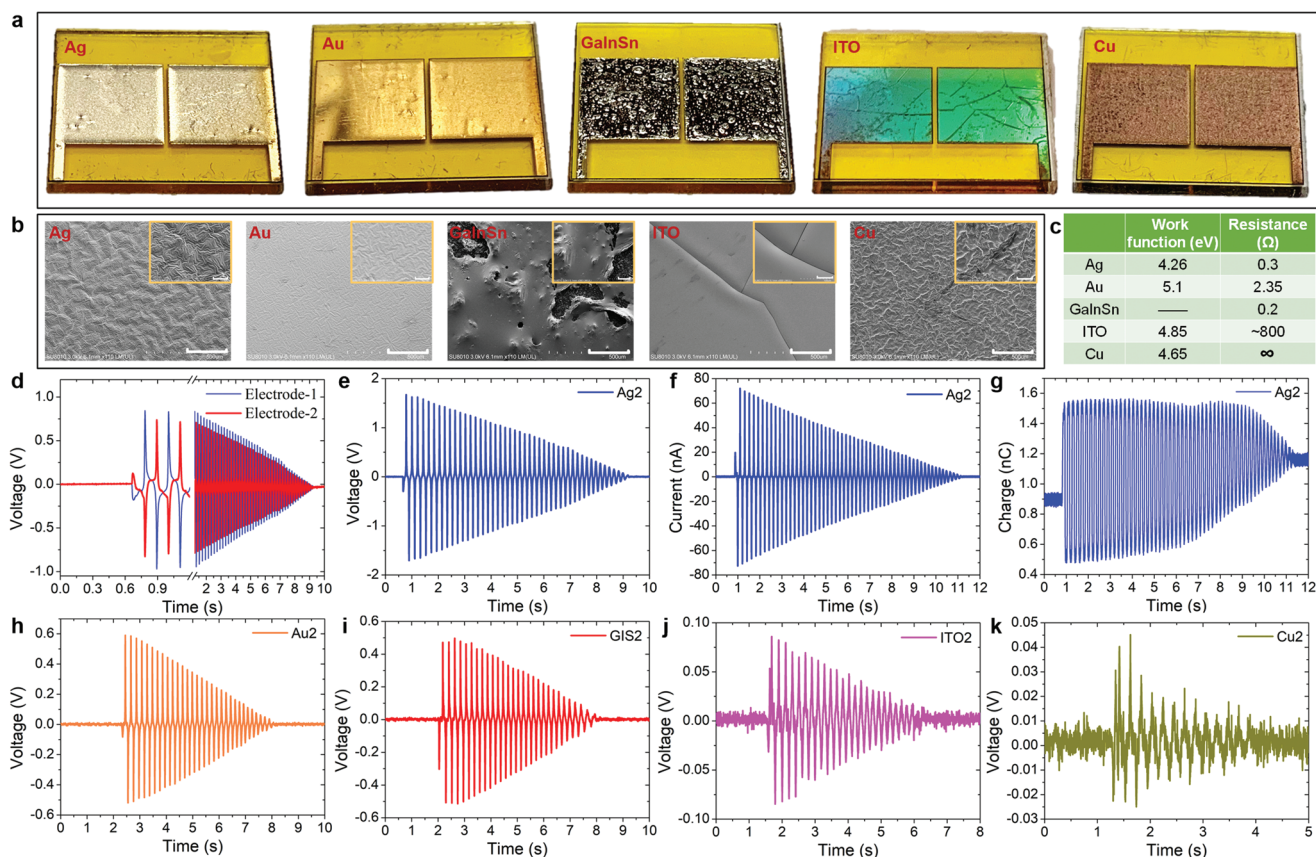
Figure 2. Effect of electrode material on the output performance of the MS. a) Photographs of the electrode materials coated on the Kapton film. b) SEM images of the electrode materials, the scales of the main and inset images are 250 and 50 µm, respectively. c) Work function and resistance of the electrode materials. d) Output waveforms of the two electrodes of Ag2. e) V_{oc}, f) I_{sc}, and g) Q_{sc} of the Ag2. h–k) V_{oc} of the Au2, GIS2, ITO2, and Cu2, respectively.

Thus, through analysis the output signals of the TENG, the excitation conditions can be detected.

The effect of electrode material on the output performance of the MS are tested and described in **Figure 2**. For preparing the electrode material of the MS, an acrylic block covered by a Kapton film with adhesive on both sides is used as a substrate. The protect film of the Kapton film is directly fabricated as an electrode mask. Then, Ag, Au, ITO, and Cu are coated by physical vapor deposition (PVD). GaInSn is a good liquid metal, which is directly scrape coated. The width and length of electrodes both are 10 mm. Their entities are shown in Figure 2a. The corresponding SEM images are described in Figure 2b. As the surface of the Kapton with adhesive is very rough, it leads the surface topography (ST) of those electrodes all are not a smooth one. In them, the Au-electrode has the best ST because it has extremely high ductility, the wrinkles on the ST of the Ag-electrode is more apparent than that of the Au-electrode, the GaInSn-electrode has the worst ST as the exiting of many holes and bubbles, and the ITO-electrode and Cu-electrode both have visible cracks. Then, the work function, which is the minimum thermodynamic work needed to remove an electron from a solid to a point in the vacuum immediately outside the solid surface, and resistance of these electrodes are recorded in Figure 2c. In addition to the unknown of GaInSn, Ag has the

smallest work function. That is to say, the Ag-electrode is most likely to lose electrons and becomes negatively charged. As the exiting of cracks, the resistances of the ITO-electrode and Cu-electrode both are very large. Even with the worst ST, due to the excellent electrical conductivity as a liquid metal, the resistance of the GaInSn-electrode is the lowest one. The MSs based on these electrodes are fabricated and recorded as Ag2, Au2, GIS2, ITO2, and Cu2, respectively. The output performance of them is tested under 10 m s^{-2} by the linear motor-based experimental setup shown in Figure S2 (Supporting Information). The two electrodes of the MS are recorded as Electrode-1 and Electrode-2, the output waveforms of which are shown in Figure 2d. The phase difference between them is 180°, which can be used to distinguish the excitation orientation. The MS exploits difference output structure of the two electrodes. Figure 2e–g is the open-circuit voltage (V_{oc}), I_{sc}, and short-circuit charge transfer (Q_{sc}) of the Ag2, respectively. These results show that the locomotion of the MC is a damping process. The peak values of the V_{oc}, I_{sc}, and Q_{sc} are about 1.75 V, 70 nA, and 1.05 nC, respectively. At the same time, the V_{oc} of Au2, GIS2, ITO2, and Cu2 are tested and described in Figure 2h–k. Compared with the V_{oc} of these MSs, the Cu2 is the worst one that is corresponding to the huge resistance of the Cu-electrode. However, even the GaInSn-electrode has the lowest resistance, the GIS2 is not the
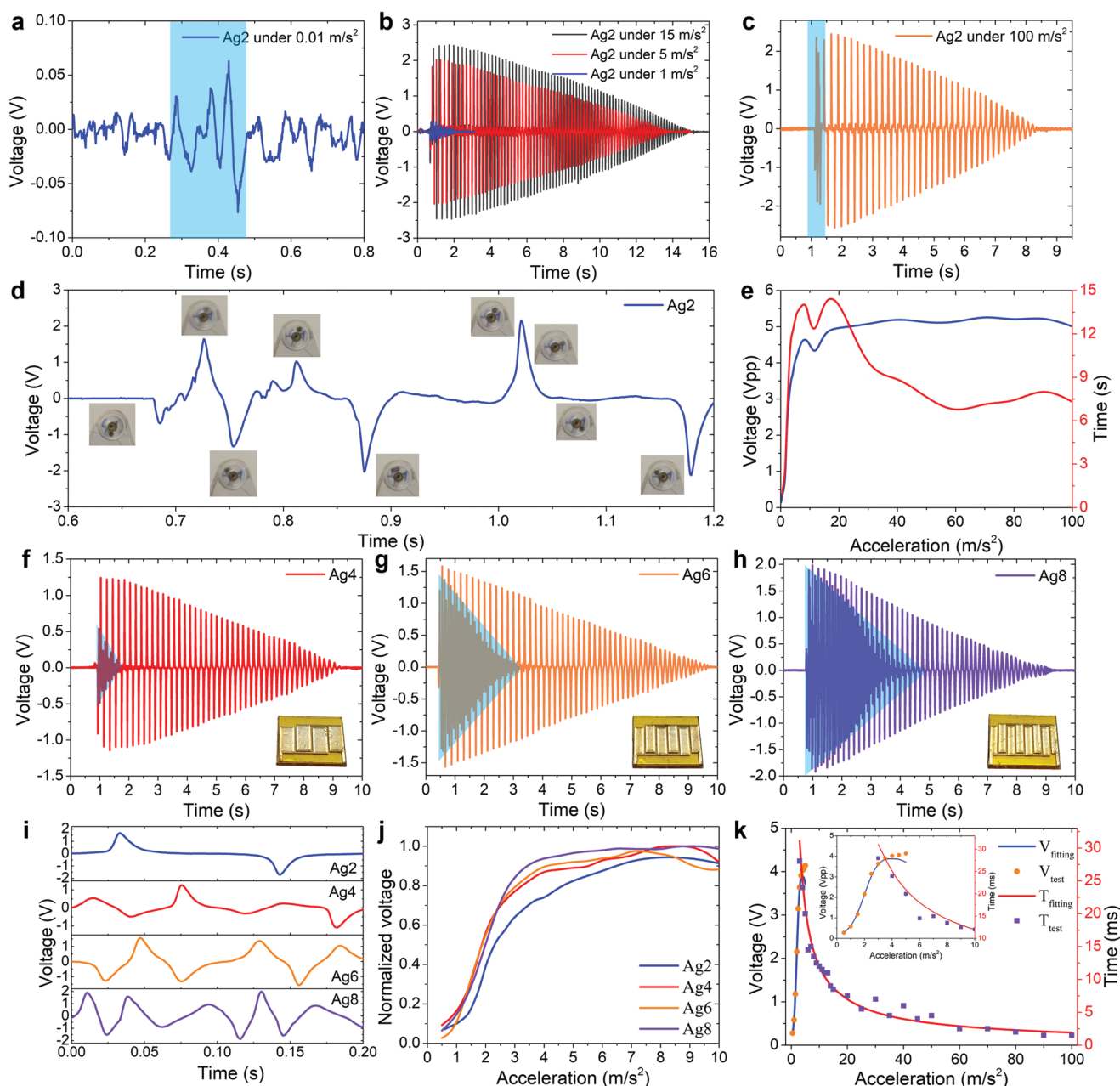
Figure 3. Output performance of the MS under different acceleration. a) V_{oc} of the Ag2 under 0.01 m s^{-2}. b) V_{oc} of the Ag2 under 1, 5, and 15 m s^{-2}. c) V_{oc} of the Ag2 under 100 m s^{-2}. d) Motion states of the MC corresponding to the waveform of the V_{oc} of the Ag2 under 100 m s^{-2}. e) Peak to peak value and lasting time of the V_{oc} of the Ag2 under different acceleration. f,g) V_{oc} of the Ag4, Ag6, and Ag8 under 10 m s^{-2}, respectively. i) Output waveforms details of the Ag2, Ag4, Ag6, and Ag8. j) Normalized voltages of the Ag2, Ag4, Ag6, and Ag8 under different acceleration. k) Peak to peak value and feature time of the V_{oc} of the Ag8 under different acceleration.

best one, which is attributed to the worst ST. The Ag2 with the lowest work function, much smaller resistance, and suitable ST is the best one. To sum up, for designing a TENG with excellent output performance, the electrode material with small work function, low resistance, and suitable ST is the best choice.

Figure 3 describes the output performance of the MS under different accelerations. When the acceleration is as low as 0.01 m s^{-2}, the Ag2 also can response to it and output a V_{oc} with the amplitude of ≈75 mV. Figure 3a demonstrates the

excellent sensitivity of the translational-rotary magnetic mechanism. With the increasing of the acceleration, not only the amplitude of the V_{oc} will be increased, but also the lasting time of the damping process will be grown, as shown in Figure 3b. The typical locomotion process of the MC under 10 m s^{-2} is recorded in Video S2 (Supporting Information). In it, the MC only does the swing motion. When the acceleration is large enough, such as the 100 m s^{-2} shown in Figure 3c and Video S3 (Supporting Information), the MC rotates first and

**ADVANCED
SCIENCE NEWS**

www.advancedsciencenews.com

**ADVANCED
ENERGY
MATERIALS**

www.advenergymat.de

then into the swing stage. The details of the MCs locomotion states corresponding to the waveform of the V_{oc} are exhibited in Figure 3d. These experimental results well confirm the theoretical analysis discussed in Figure 1. Then, the peak to peak value and lasting time of the V_{oc} of the Ag2 under different accelerations are extracted and plotted in Figure 3e. When the acceleration is smaller than about 10 m s^{-2}, they have approximately linear relationships with the acceleration. But using them to distinguish the acceleration larger than 10 m s^{-2} will not be so effective. To solve this problem, the pairs of IEs are increased to 2, 3, and 4 in turn, the corresponding MSs are recorded as Ag4, Ag6, and Ag8, respectively. Figure 3f–h shows the entities and the V_{oc} of the Ag4, Ag6, and Ag8 under 10 m s^{-2}, respectively. With increasing the pairs of IEs, there are a little fluctuation of the V_{oc}'s amplitude, but the frequency of which increases sharply, just like the enlarging of the triangle area shown in these figures. This is further described in Figure 3i. During the same time, the cycle's number of Ag2, Ag4, Ag6, and Ag8 multiply with the increasing of the pairs of IES. During the whole damping process, the relationship between the number of cycles and the acceleration is recorded in Figure S3 (Supporting Information). Furthermore, the normalized voltages of the Ag2, Ag4, Ag6, and Ag8 under different accelerations are described in Figure 3j. Under a small acceleration, which is specified as 4 m s^{-2}, the Ag8 has the largest output voltage. So, the Ag8 has the biggest slope, which provides the highest sensitivity. The sensitivity of Ag 6 is a little larger than that of Ag4. This is caused by the installation error of the translational-rotary magnetic mechanism. The center plane of the MD is not perpendicular to the tube, and then the motion locus of the MC will be deflected, which will directly influence the output performance of the MS. Thus, the Ag8 is specified to measure the acceleration in the following. As shown in Figure 3j,k, the peak to peak value of the V_{oc} has an approximately linear relationship with the acceleration during it is less than 4 m s^{-2}, which is corresponding to the length of the interdigital. With the acceleration larger than 4 m s^{-2}, the MC will be driven to pass through an interdigital into another one, then a peak or a valley can be got from the V_{oc}. Thus, a feature time corresponding to this can be extracted to calculate the larger acceleration, as shown in Figure 3k.

Compared the waveforms of the V_{oc} of different electrode materials, the ratios between the amplitude of the first valley and the amplitude of the V_{oc} are difference. This is caused by the dip angle of the MS, the schematic diagram of which is shown in Figure S4a (Supporting Information). A linear motor-based inclination experimental setup shown in Figure S4b (Supporting Information) is established to test the output performance of the Ag2 under different dip angles, which is adjusted by a small turntable. The first peak and valley of the V_{oc} under some typical dip angles are shown in **Figure 4**a. With the increasing of the dip angle, the amplitude of the peak is increased, the feature time between the peak and valley is decreased, as plotted in Figure S5 (Supporting Information). But when the dip angle is larger than 70°, the amplitude of the peak decreases sharply. According to the structure characteristic of the translational-rotary magnetic mechanism, the MS can be used to measure the rotational parameters without the need of coaxial installation. A servo motor-based experimental

setup shown in Figure S6 (Supporting Information) is build and the test results are shown in Figure S7 (Supporting Information). The frequency of the V_{oc} is linear proportional to the rotational speed.

To verify the feasibility and efficiency of the acceleration testing, two MSs are embedded in the boxing gloves and used to measure the punch acceleration, as shown in Figure 4b and Video S4 (Supporting Information). In Figure 4c, the average punch acceleration of the right glove is larger than that of the left glove, which is corresponding to the dominant hand of the tester is right. The maximum punch acceleration of the right glove is up to 30 m s^{-2}. In Figure 4d, the MS is placed on the ball head of a golf club to measure the hitting force, the ball is attached with a force sensor fixed on the desk. The hitting process under different states is recorded in Video S5 (Supporting Information). The waveforms of the V_{oc} and the corresponding forces are described in Figure 4e. When the hitting force is as low as 0.80 N, a waveform with the amplitude of 0.4 V can be got from the MS. It further confirms the outstanding sensitivity of the MS. When the hitting force increases up to 15 N, the MS also will start with the rotating stage and then into the swing stage, as shown in Figure 4f. Based on the MS, the swing angle of golf also has been tested by the Ag8, as shown in Figure 4g and Video S6 (Supporting Information). When swing the golf club, it will provide an initial rotate stage to the MS that is corresponding to the swing angle, just like the time interval less than 0.7 s shown in Figure 4h. In this interval, the number of cycles of the V_{oc} is directly proportional to the swing angle. Then, after deal with a zero-crossing comparator, the swing angle can be easily detected by counting the number of pulses. So, through increasing the number of the pairs of IES, the resolution and sensitivity of the MS can be significantly enhanced. Due to the MS can easily respond to a weak striking, it has also been used to develop a vehicle safety application, as shown in Figure S5i and Video S7 (Supporting Information). The MS is fixed on the handle of a vehicle to detect the action of the handle. For enhancing the efficiency of the vehicle safety application, an infrared sensor is placed near the handle to distinguish the present of the hand. When the vehicle is locked, if a hand tries to pull the handle, an alarm of the application will sound.

A translational-rotary triboelectric nanogenerator-based multifunctional sensor has been proposed to detect acceleration, force, and rotational parameters. The translational-rotary magnetic mechanism is formed by a low damping MC rotating around a fixed circular friction tube, which is embedded by an MD. The MS can transform a translational motion into a swing motion or a multicircle rotational motion of the MC around the friction tube and hence drives the TENG to generate voltages output. The output performance of the MS with different electrode materials and different number of the pairs of IEs has been systematically studied and tested. It indicates that the electrode material with small work function, low resistance, and suitable surface topography is the best choice to improve the output performance of the TENG. With the increasing of the pairs of IEs, the resolution and sensitivity of the MS can be enhanced significantly. Based on the MS, some applications have been established to measure the punch acceleration of the boxing, the hitting force and swing angle of the golf, which
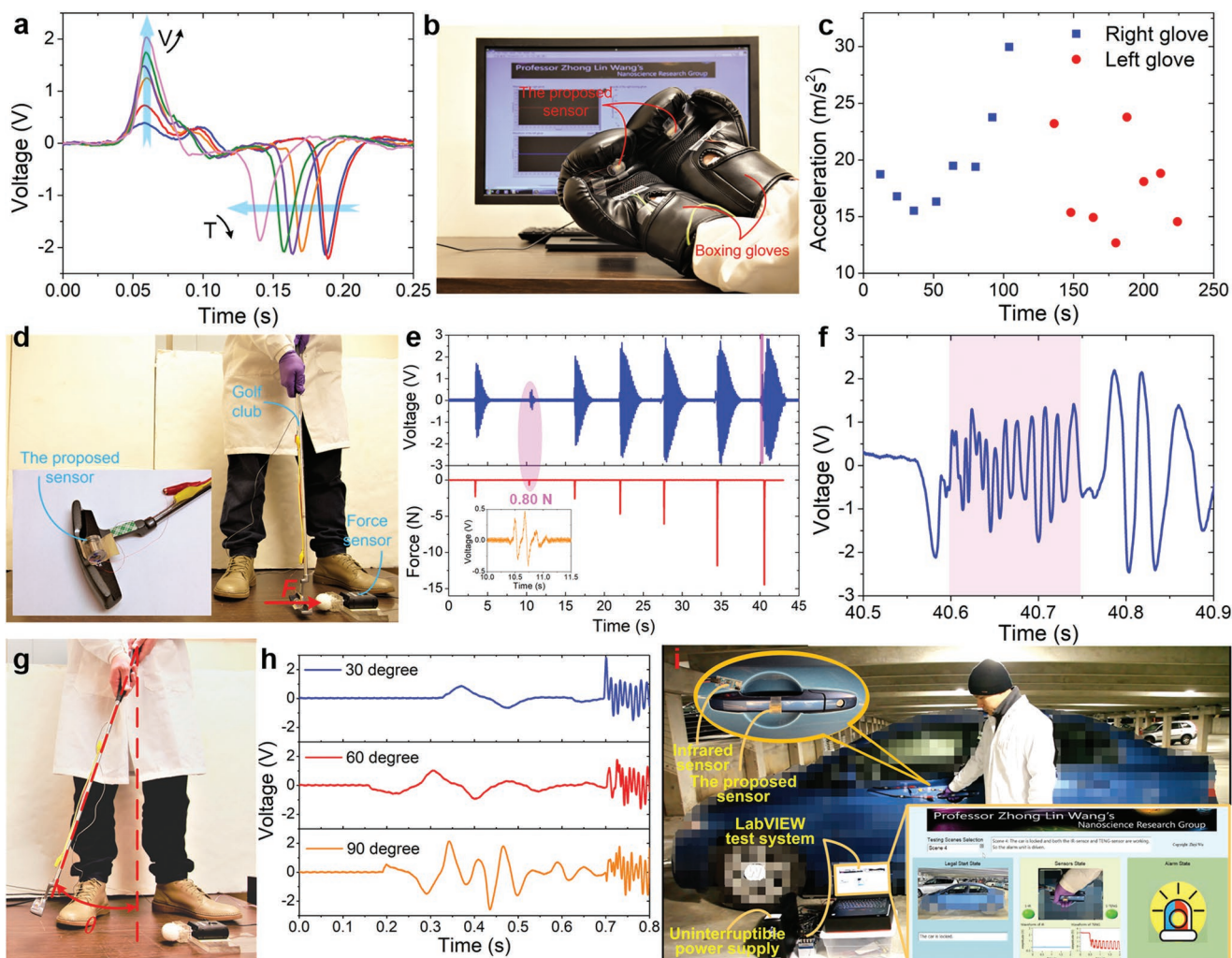
**ADVANCED
SCIENCE NEWS**
www.advancedsciencenews.com

**ADVANCED
ENERGY
MATERIALS**
www.advenergymat.de

Figure 4. Applications of the MS. a) The first peak and valley of the V_{oc} under different dip angle of Ag2. b) Punch acceleration application of boxing. c) Acceleration test results of the right and left gloves, respectively. d) Hitting force application of golf. e) Corresponding results between the V_{oc} of the MS and the hitting force. f) Waveform details of the V_{oc} the under ≈15 N. g) Swing angle application of golf. h) Waveforms of the V_{oc} under 30°, 60°, and 90°, respectively. i) Vehicle safety application.

demonstrate the feasibility and efficiency of the MS and exhibit that the MS can have important application in sports. Cooperated with an infrared sensor, the MS has been used to develop a vehicle safety application. When some unauthorized person tries to pull the handle of the vehicle, the alarm of the application will sound. According to the structure characteristic of the translational-rotary magnetic mechanism, the MS can easily respond to a weak striking and can be used to measure the rotational parameters without the need of coaxial installation. This provides the MS a good application prospect in mechanical control and robots and other applications that require motion feedback.

Experimental Section

Fabrication of the Electrodes: For prepare the electrode material of the MS, an acrylic block covered by a Kapton film with adhesive on both sides was used as the substrate. The acrylic block with the diameters of 20.45 mm × 19 mm was fabricated by a laser cutter (PLS6.75, Universal Laser Systems) from an acrylic plate with the thickness of 0.063 in. The protect film of the Kapton film (McMaster-Carr, thickness: 0.0056 in.) was directly fabricated as the electrode mask by the laser cutter. Ag, Au, and Cu were coated via the Denton Explorer E-beam Evaporator (CHA E-beam Evaporator). The thicknesses of the coating layer were 200 nm with a coating speed of 2 Å s⁻¹. The ITO was coated by the Kurt J. Lesker physical PVD (PVD75 RF Sputterer) RF 75 Sputterer with a power of 100 W under the pressure of 5 mTorr with a constant flow rate of 40 sccm of Ar for 40 min. The thickness was about ≈200 nm. The GaInSn was directly scrape coated by hand. Then, removing the masks, the electrodes were prepared, the width and the length of which both are 10 mm. The surface topography of those electrodes was tested by Hitachi SU8010 SEM.

Fabrication of the Friction Layer: A PTFE thin film (McMaster-Carr, thickness: 0.002 in. and 0.0015 in., respectively) was cleaned and cut into rectangular with diameters of 20.45 mm × 19 mm by the laser cutter. Then, the PTFE film was covered on the electrodes to make the friction layer.

Fabrication of the Shell: The shell contains two tubes and two covers. The acrylic cover with the diameters of 15.88 mm × 6.65 mm was fabricated by the laser cutter from an acrylic plate with the thickness of

**ADVANCED
SCIENCE NEWS**

www.advancedsciencenews.com

**ADVANCED
ENERGY
MATERIALS**

www.advenergymat.de

0.063 in. The acrylic tubes with the height of 19 mm are cut out from long tubes by a hand-held grinding wheel. The diameters of the tubes are 19 mm × 15.9 mm and 6.6 mm × 5.1 mm, respectively.

Assembling of the Proposed Sensor: The friction layer was stripped from the acrylic substrate and then wrapped around the small tube. The magnetic disk was embedded in the small tube. The magnetic cylinder was adsorbed beside the small tube by the magnetic force between the magnets. This is the core of the sensor, the performance of which can be improved by adjusting the place of the magnetic disk. Finally, the sensor was prepared by packaged the core with the big tube and two covers.

Testing Process of the V_{oc}, I_{sc}, and Q_{sc}: The V_{oc} is directly tested by a LabVIEW testing system, which is consisted of an NI PXI-6229 data acquisition card, a LabVIEW testing program, and a PC. The I_{sc} and Q_{sc} are measured by an electrometer (KEITHLEY Model 6514 system electrometer) and then acquired and processed by the LabVIEW testing system.

Supporting Information

Supporting Information is available from the Wiley Online Library or from the author.

Conflict of Interest

The authors declare no conflict of interest.

[1] D. Son, J. Lee, S. Qiao, R. Ghaffari, J. Kim, J. E. Lee, C. Song, S. J. Kim, D. J. Lee, S. W. Jun, *Nat. Nanotechnol.* **2014**, *9*, 397.

[2] Q. Hua, J. Sun, H. Liu, R. Bao, R. Yu, J. Zhai, C. Pan, Z. L. Wang, *Nat. Commun.* **2018**, *9*, 244.

[3] X. Liao, Q. Liao, Z. Zhang, X. Yan, Q. Liang, Q. Wang, M. Li, Y. Zhang, *Adv. Funct. Mater.* **2016**, *26*, 3074.

[4] J. S. Lee, K.-Y. Shin, O. J. Cheong, J. H. Kim, J. Jang, *Sci. Rep.* **2015**, *5*, 7887.

[5] L. Zhang, L. Jin, B. Zhang, W. Deng, H. Pan, J. Tang, M. Zhu, W. Yang, *Nano Energy* **2015**, *16*, 516.

[6] L. Shuangfeng, M. Tiehua, H. Wen, *Sens. Actuators, A* **2008**, *147*, 70.

[7] C. C. Hindrichsen, N. S. Almind, S. H. Brodersen, R. Lou-Møller, K. Hansen, E. V. Thomsen, *J. Electroceram.* **2010**, *25*, 108.

[8] H. C. Lefevre, *The Fiber-Optic Gyroscope*, Artech House, Norwood, MA **2014**.

[9] Z. Nussinov, J. Van Den Brink, *Rev. Mod. Phys.* **2015**, *87*, 1.

[10] Z. Wu, Y. Wen, P. Li, *IEEE Trans. Energy Convers.* **2013**, *28*, 921.

[11] S. Priya, D. J. Inman, *Energy Harvesting Technologies*, Springer, Berlin **2009**.

[12] Z. Wu, J. Tang, X. Zhang, Z. Yu, *Appl. Phys. Lett.* **2017**, *111*, 013903.

[13] S. H. Kim, C. S. Haines, N. Li, K. J. Kim, T. J. Mun, C. Choi, J. Di, Y. J. Oh, J. P. Oviedo, J. Bykova, *Science* **2017**, *357*, 773.

[14] Z. L. Wang, *Nature* **2017**, *542*, 159.

[15] J. Wang, S. Li, F. Yi, Y. Zi, J. Lin, X. Wang, Y. Xu, Z. L. Wang, *Nat. Commun.* **2016**, *7*, 12744.

[16] Z. L. Wang, *Nano Energy* **2019**, *58*, 669.

[17] Y. Nemirovsky, A. Nemirovsky, P. Muralt, N. Setter, *Sens. Actuators, A* **1996**, *56*, 239.

[18] Z. L. Wang, *Nano Today* **2010**, *5*, 512.

[19] F.-R. Fan, Z.-Q. Tian, Z. L. Wang, *Nano Energy* **2012**, *1*, 328.

[20] Z. L. Wang, *ACS Nano* **2013**, *7*, 9533.

[21] Z. L. Wang, *Faraday Discuss.* **2015**, *176*, 447.

[22] L. Zhang, B. Zhang, J. Chen, L. Jin, W. Deng, J. Tang, H. Zhang, H. Pan, M. Zhu, W. Yang, *Adv. Mater.* **2016**, *28*, 1650.

[23] S. Wang, L. Lin, Z. L. Wang, *Nano Energy* **2015**, *11*, 436.

[24] P.-K. Yang, Z.-H. Lin, K. C. Pradel, L. Lin, X. Li, X. Wen, J.-H. He, Z. L. Wang, *ACS Nano* **2015**, *9*, 901.

[25] Q. Jing, G. Zhu, W. Wu, P. Bai, Y. Xie, R. P. S. Han, Z. L. Wang, *Nano Energy* **2014**, *10*, 305.

[26] J. Wang, W. Ding, L. Pan, C. Wu, H. Yu, L. Yang, R. Liao, Z. L. Wang, *ACS Nano* **2018**, *12*, 3954.

[27] Y. K. Pang, X. H. Li, M. X. Chen, C. B. Han, C. Zhang, Z. L. Wang, *ACS Appl. Mater. Interfaces* **2015**, *7*, 19076.

[28] B. Zhang, L. Zhang, W. Deng, L. Jin, F. Chun, H. Pan, B. Gu, H. Zhang, Z. Lv, W. Yang, *ACS Nano* **2017**, *11*, 7440.

[29] H. Wu, Z. Su, M. Shi, L. Miao, Y. Song, H. Chen, M. Han, H. Zhang, *Adv. Funct. Mater.* **2018**, *28*, 1704641.

[30] Y. Wu, Q. Jing, J. Chen, P. Bai, J. Bai, G. Zhu, Y. Su, Z. L. Wang, *Adv. Funct. Mater.* **2015**, *25*, 2166.

[31] K. Dong, Z. Wu, J. Deng, A. C. Wang, H. Zou, C. Chen, D. Hu, B. Gu, B. Sun, Z. L. Wang, *Adv. Mater.* **2018**, *30*, 1804944.

[32] Z. Lin, Z. Wu, B. Zhang, Y. C. Wang, H. Guo, G. Liu, C. Chen, Y. Chen, J. Yang, Z. L. Wang, *Adv. Mater. Technol.* **2019**, *4*, 1800360.

[33] Z. Wu, W. Ding, Y. Dai, K. Dong, C. Wu, L. Zhang, Z. Lin, J. Cheng, Z. L. Wang, *ACS Nano* **2018**, *12*, 5726.

[34] Z. L. Wang, J. Chen, L. Lin, *Energy Environ. Sci.* **2015**, *8*, 2250.

[35] C. Wu, A. C. Wang, W. Ding, H. Guo, Z. L. Wang, *Adv. Energy Mater.* **2019**, *9*, 1802906.

[36] H. Zou, Y. Zhang, L. Guo, P. Wang, X. He, G. Dai, H. Zheng, C. Chen, A. C. Wang, C. Xu, Z. L. Wang, *Nat. Commun.* **2019**, *10*, 1427.